Designing a Transition Photonic Band with a Moiré Synthetic Sphere

Z.N. Liu,[1] X.Q. Zhao,[1] J. Yao,[2] C. Zhang,[1] J.L. Xu,[1] S Zhu,[1] and H. Liu[1,*]

[1] *National Laboratory of Solid State Microstructures, School of Physics, Collaborative Innovation Center of Advanced Microstructures, Nanjing University, Nanjing 210093, China*

[2] *Department of Materials Science and Engineering, University of California, Berkeley, California 94720, USA*

(Received 13 October 2022; revised 16 February 2023; accepted 21 March 2023; published XX XX 2023)

In recent years, twisted bilayer graphene has become a hot topic and inspired the upsurge of research on the photonic moiré lattice. Here, we design a photonic moiré superlattice with two synthetic twist angles and construct a synthetic moiré sphere based on these two angles. Thus, we have more degrees of freedom to design the band structure flexibly. A type of transition photonic band (TPB) is obtained in such a moiré superlattice. We investigate the influence of two twist angles on TPBs and find a series of magic angle pairs with optimal band compression of the TPB. Interesting optical properties of TPBs are experimentally demonstrated, including pulse delay, nonlinear optical enhancement, and pulse-width compression. Our work introduces an alternative path to explore multitwist-angle moiré superlattices and reveals that the designed photonic moiré superlattice based on moiré spheres has broad application prospects, including optical signal processing, nonlinear optic processes, and other light-matter interactions.

DOI: 10.1103/PhysRevApplied.0.XXXXXX

I. INTRODUCTION

A moiré lattice is a composite structure formed by the overlap of two identical or similar periodic structures [1]. Recently, in twisted double-layer graphene, it was found that, at the so-called magic angle, the band appeared as a flat band near the Fermi level, and there was a nontrivial topological phase [2–4]. Moreover, double-layer graphene exhibits the Mott insulating phase and a superconducting phase [5–8]. Meanwhile, the moiré lattice brings the possibility of exotic physics phenomena, including moiré excitons [9], fractional Chern insulators [10], and lattices with competing periodicities [11].

On the other hand, moiré lattices also introduce interesting physical effects in photonic systems [1,12,13]. In particular, moiré fringes are applied to metal surfaces to modulate plasmonic dispersion and group velocity [13]. In a two-dimensional photonic moiré lattice, the localization-delocalization transition of light is realized experimentally [14]. The tunable topological transitions and phonon polaritons are achieved in bilayers of α-phase molybdenum trioxide (α-MoO_3) [15,16]. The formation of optical solitons are controlled by the twist angle in photonic moiré lattices [17,18] and magic angle lasers in the nanostructured moiré lattice exhibit salient features [19]. Recently, a coupled-mode theory for low-angle twisted bilayer honeycomb photonic lattices reveals a correspondence between fermionic and bosonic moiré systems [20]. Also, the so-called magic distance is found in the bilayer photonic moiré lattice. Meanwhile, slow light, nonlinear effects, chiral plasmons, thermal emitters, and filters exhibit excellent properties in the photonic moiré lattice system [21,22]. One major attraction of these structures is that their optical properties are strongly dependent on the twist angle. However, up to now, in most reported works, the bands of moiré lattices are tuned by changing a single twist angle. The degree of freedom of a single twist angle is very limited. In most moiré structures, it is difficult to find interesting physical properties by adjusting a single twist angle. Fortunately, synthetic parameters allow us to explore physical phenomena in high-dimensional synthetic space [23–33]. Inspired by this method, we introduce synthetic twist angles into the moiré system.

Here, we propose a moiré superlattice with two synthetic twist angles, in which a kind of transition photonic band (TPB) is obtained. A two-dimensional synthetic moiré sphere is constructed based on these two synthetic twist angles. The twist angles are tuned to design the moiré lattice. A series of magic angle pairs on the moiré sphere are found to obtain TPBs with optimal band compression. Experimentally, we directly investigate the properties of TPBs, including narrowband filtering, pulse delays, nonlinear optical enhancement, and pulse-width compression.

II. DESIGN OF PHOTONIC MOIRÉ SUPERLATTICES BASED ON SYNTHETIC MOIRÉ SPHERES

First, let us consider a simple photonic lattice, which has two refractive-index layers of equal thickness, n_a and n_b, in

*liuhui@nju.edu.cn

a unit cell, the refractive-index distribution of which can be characterized as

$$V_\Lambda(z) = \sin\left(\frac{2\pi}{\Lambda} + \frac{\pi}{2}\right), \tag{1}$$

where Λ is the spatial period and z is the spatial location. When the spatial position is $V_\Lambda(z) > 0$, the refractive-index distribution function is $n_\Lambda(z) = n_a$; otherwise, $n_\Lambda(z) = n_b$. To illustrate the idea of the moiré superlattice, we consider a one-dimensional superlattice composed of two simple photonic lattices with different periods, Λ_1 and Λ_2. The moiré superlattice can be expressed as

$$P_\Lambda(z) = \sin^2\frac{\gamma}{2} V_{\Lambda_1}(z) + \cos^2\frac{\gamma}{2} V_{\Lambda_2}(z), \tag{2}$$

where $\gamma \in (0, 180^\circ)$, $V_{\Lambda_1}(z)$ and $V_{\Lambda_2}(z)$ are the simple lattice structure functions, and $P_\Lambda(z)$ is the moiré superlattice structure function. When $P_\Lambda(z) > 0$, the refractive index equals n_a; otherwise, it equals n_b. In general, Λ_1 and Λ_2 vary continuously. When Λ_1 and Λ_2 are incommensurable, the moiré superlattice is not periodic, and the band cannot be obtained by Bloch's theorem. Therefore, we consider the case where Λ_1 and Λ_2 are commensurable, i.e., $\Lambda_1/\Lambda_2 = m/n$, where m and n are positive integers. Then, the period of the superlattice is $\Lambda = n\Lambda_1 = m\Lambda_2$. If Λ_1 and Λ_2 are changed and the ratio of Λ_1/Λ_2 remains unchanged, the bands only shift in wavelength, but the band configuration does not change. Therefore, the band configuration is mainly determined by the ratio of m/n. Here, we can define the synthetic twist angle as $\alpha = 8 \times \arctan(m/n)$, which plays an important role in

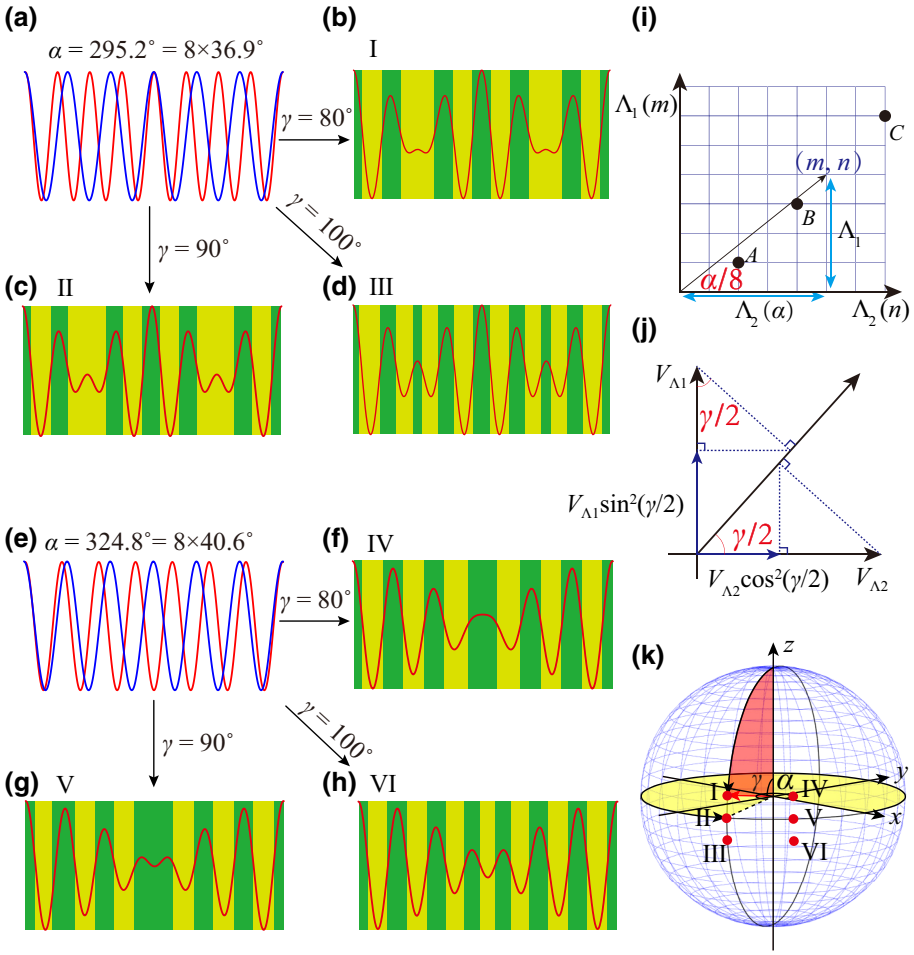

FIG. 1. (a),(e) Red and blue lines characterize two simple lattices. (a) Periodic ratio of the red line to the blue line is 3/4. (e) Periodic ratio of the red line to the blue line is 6/7. (b)–(d),(f)–(h) Structures I (295.2°, 80°), II (295.2°, 90°), III (295.2°, 100°), IV (324.8°, 80°), V (324.8°, 90°), and VI (324.8°, 100°), respectively. Red lines are the characterization function, and background is a schematic of the refractive-index distribution. (i) Synthetic angle α in the parameter space (Λ_1, Λ_2). Black dots are parameters of the experimental sample. (j) Synthetic angle γ in the parameter space ($V_{\Lambda_1}(z)$, $V_{\Lambda_2}(z)$). (k) Synthetic moiré sphere defined with two synthetic angles (α, γ) and the superlattice defined with synthetic angles (red curve) I (295.2°, 80°), II (295.2°, 90°), III (295.2°, 100°), IV (324.8°, 80°), V (324.8°, 90°), and VI (324.8°, 100°).

tuning the band configuration. In Fig. 1(i), α is shown as a synthetic angle in the parameter space (Λ_1,Λ_2) visually. The line passing through the lattice point, the angle of which with the Λ_2 axis of $\alpha/8$ represents a periodic moiré superlattice. Otherwise, the line with angle $\alpha/8$ that does not pass through any lattice point represents a nonperiodic moiré superlattice. In Fig. 1(j), γ can also be represented as a synthetic angle in the parameter space ($V_{\Lambda_1}(z)$, $V_{\Lambda_2}(z)$). The structure functions of two simple photonic lattices as basis vectors ($V_{\Lambda_1}(z)$, $V_{\Lambda_2}(z)$) construct the synthetic parameter space. $\gamma/2$ can be represented as the spatial twist angle in the synthetic parameter space, as marked by red letters in Fig. 1(j). $\sin^2(\gamma/2)V_{\Lambda_1}(z)$ and $\cos^2(\gamma/2)V_{\Lambda_2}(z)$ can be obtained by two triangular transformations of the two basis vectors, $V_{\Lambda_1}(z)$ and $V_{\Lambda_2}(z)$, to the line with the angle $\gamma/2$ to the $V_{\Lambda_2}(z)$ axis. The projection of the basis vector, $V_{\Lambda_2}(z)$, to the line at an angle of $\gamma/2$ becomes $\cos(\gamma/2)V_{\Lambda_2}(z)$ and then to the basis vector of $V_{\Lambda_2}(z)$ becomes $\cos^2(\gamma/2)V_{\Lambda_2}(z)$. Meanwhile, the sine of the basis vector of $V_{\Lambda_2}(z)$ to the line at angle γ becomes $\sin(\gamma/2)V_{\Lambda_1}(z)$ and then to the basis vector of $V_{\Lambda_1}(z)$ becomes $\sin^2(\gamma/2)V_{\Lambda_1}(z)$. Therefore, $\gamma/2$ represents the proportion of the combined moiré superlattice occupied by the two initial lattice structures, $V_{\Lambda_1}(z)$ and $V_{\Lambda_2}(z)$. When $\gamma = 0$ or $\gamma = 180°$, the moiré superlattice changes back to the original simple periodic photonic lattice structure. In the method, we design six superlattices as examples with two synthetic angles. For $\alpha = 295.2°$ and 324.8°, $V_{\Lambda_1}(z)$ and $V_{\Lambda_2}(z)$ are given as the red and blue lines in Figs. 1(a) and 1(e), respectively. For $\gamma = 80°$, 90°, and 100°, $P_\Lambda(z)$ are represented as red lines in Figs. 1(b)–1(d) and 1(f)–1(h). In fact, the moiré superlattice structures are well defined by two synthetic angles (α, γ). Therefore, we can construct a two-dimensional synthetic parameter space based on these two angles. In Fig. 1(k), there are two degrees of freedom on the sphere: angle α with the x axis in the horizontal plane and the angle γ with the z axis. In this way, all the structures of superlattices can be well defined by the points on the sphere. Here, we can call this parameter space a synthetic moiré sphere.

III. TRANSITION PHOTONIC BANDS OF MOIRÉ SUPERLATTICES

To analyze the effect of the synthetic twist angles on the bands, the bands of the moiré superlattices are calculated with the transfer matrix. A superlattice is taken as an instance with $\alpha = 237.6° = 8 \times \arctan(4/7)$ and $\Lambda = 7\Lambda_1 = 4\Lambda_2$. Its band structure is investigated with $0 < \gamma < 180°$ in the Brillouin zone $(0, 2\pi/\Lambda)$. For $\gamma = 0$ and 180°, the superlattices are periodic lattices with Λ_1 and Λ_2, the bands of which are given in Figs. 2(a) and 2(c) and show band folding at the boundary of the Brillouin zone. In Fig. 2(b), the change of the band structures with γ is given as the band projection, the degeneracy introduced by band

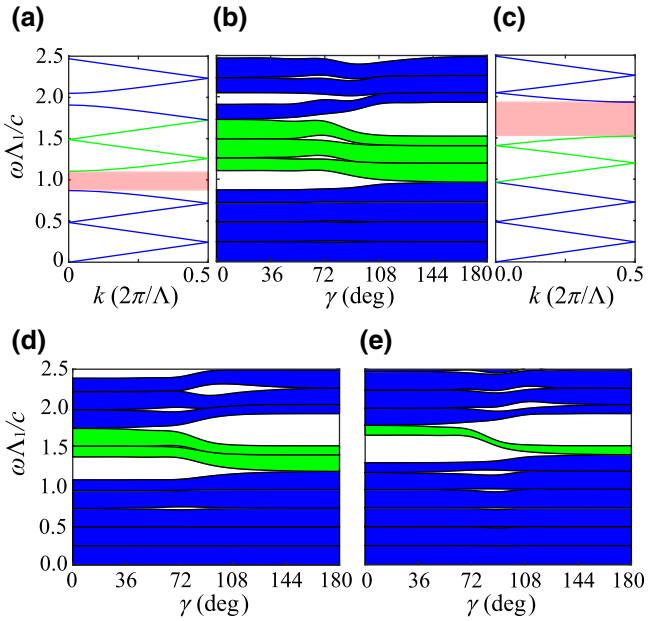

FIG. 2. Bands of simple lattices with (a) $\Lambda_1 = \Lambda/7$, $\gamma = 180°$ and $\Lambda_2 = \Lambda/4$, $\gamma = 180°$ in the Brillouin zone $(0, 2\pi/\Lambda)$. Pink shaded area is the first band gap, and green line is TPB. Dependence of band projections of the superlattice with (b) $\alpha = 237.6°$, (d) 284°, (e) 324.8° on γ.

folding is lifted, and a band gap emerges at two boundaries of the Brillouin zone. The three bands (marked in green) above the first gap [marked in pink in Fig. 2(a)] on the left boundary ($\gamma = 0$) are shifted to the bands below the first gap [marked in pink in Fig. 2(c)] on the right boundary ($\gamma = 180°$). Here, we call the green bands TPBs. For comparison, we show the band projections of two superlattices with $\alpha = 284° = 8 \times \arctan(5/7)$ ($m = 5$, $n = 7$) and $\alpha = 324.8° = 8 \times \arctan(6/7)$ ($m = 6$, $n = 7$) in Figs. 2(d) and 2(e). There are two TPBs in Fig. 2(d) and one TPB in Fig. 2(e). Obviously, the number of TPBs is determined by $|n - m|$, which is understood from band folding at the two boundaries. It is worth stating that, for the case of $|n - m| > 1$, several TPBs are very close to each other and the gaps between TPBs are very small. In a practical system, they are very easily merged together if the sample length is not large enough. However, for the case of $|n - m| = 1$, we can obtain a single isolated TPB with narrow frequency intervals, even for a sample with only a few periods. Therefore, the isolated TPB is more useful for practical applications. In the following, we focus only on the structures of $|n - m| = 1$.

Tuning the photonic bandwidth is an important means of manipulating light. For example, applications often require narrowband filtering in transmission, and band flattening due to band compression achieves slow light and affects the group-velocity dispersion. Therefore, the

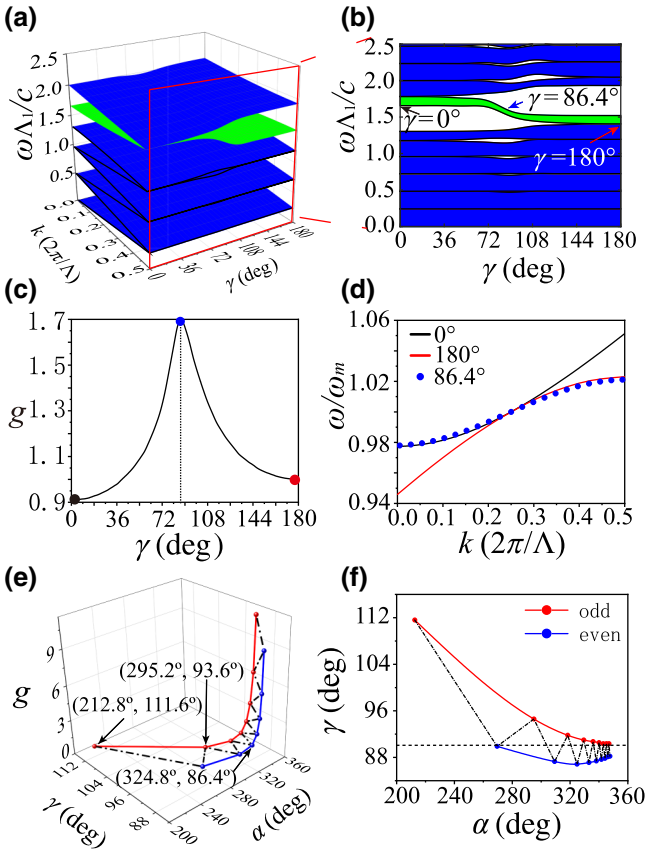

F3:1 FIG. 3. (a) Bands of superlattice with $\alpha = 324.8°$ and
F3:2 $0 < \gamma < 180°$, and green surface is the TPB. (b) Band projec-
F3:3 tion on the plane (ω, γ). (c) Change of g on γ. (d) Three bands
F3:4 of $\gamma = 0°$, 86.4°, and 180°, and ω_m is the midband position. (e)
F3:5 Series g_M with magic angle pairs (α_M, γ_M). (f) Two asymptotic
F3:6 curves of magic angles when m is odd (red curve) and m is even
F3:7 (blue cure).

tunability of the TPB bandwidth can be applied to manipulate light. To investigate the dependence of TPB bandwidth on γ, we define the compression coefficient as $g = (\text{band}(\gamma = 180°)/\text{band}(\gamma))$, where band$(\gamma)$ is the TPB bandwidth with γ. Obviously, a larger g leads to a narrower TPB bandwidth. The varying bands of the superlattice ($\alpha = 324.8°$) with γ are given in Fig. 3(a), and the projection of these bands on the (ω, γ) plane is given in Fig. 3(b). The TPB is marked in green in both Figs. 3(a) and 3(b). The optimal bandwidth compression of the TPB can be found by tuning γ. As shown in Fig. 3(c), when $\gamma = 86.4°$, g reaches a maximum and the TPB bandwidth reaches a minimum. In Fig. 3(d), the TPB at $\gamma = 86.4°$ (blue dots) is compared with the TPBs at $\gamma = 0$ (black curve) and 180° (red curve), and it has a narrower bandwidth than in the other two cases. Apart from the TPB, several bands near the TPB will also be compressed (see the Supplemental Material, Sec. 1 [34]). This means the TPB is different from the resonance defect mode.

In the above discussion, we find that g is determined by both α and γ simultaneously. Therefore, we investigate the dependence of g on the synthetic moiré sphere (α, γ). For each α_M, we can find the optimal compression coefficient, g_M, at certain γ_M. Here, the corresponding angle pairs (α_M, γ_M) found can be defined as magic angle pairs, as shown in Table I. In Fig. 3(e), we plot the change in g_M for a series of magic angle pairs. As α_M approaches 360°, g_m is increased to infinity. However, if α equals 360°, the two periods are equal $(\Lambda_1 = \Lambda_2)$. Then the superlattices will change back to a simple periodic lattice, and the TPB disappears. Moreover, to show the distribution of magic angle pairs, we project the three-dimensional spatial curve onto the two-dimensional plane [see Fig. 3(f)]. It is obvious that (α_M, γ_M) are located at two asymptotic curves. When m is odd, γ_M approaches 90° along the red curve, and when m is even, γ_M approaches 90° along the blue curve. Besides, we also investigate the dependence of TPBs on the incidence angle (Supplemental Material, Sec. 2 [34]). For the TE mode, the results show that the bandwidth of the TPB decreases with k_y increasing. For the TM mode, the results show that the bandwidth of the TPB widens with k_y increasing. This causes the group indices of the two modes to change in opposite directions (Supplemental Material, Sec. 3 [34]).

IV. EXPERIMENTAL OBSERVATION OF TRANSITION PHOTONIC BANDS

We fabricate three moiré superlattices, A (212.8°, 111.6°), B (295.2°, 93.6°), and C (324.8°, 86.4°), which are marked as dots in Fig. 1(i). Figure 4(a) shows a SEM microscopy picture of sample C. The TPB bandwidths of the three samples are found to be 479, 117, and 31 nm. With α increasing, its transmission bandwidth is reduced (see the Supplemental Material, Sec. 2 [34]), which agrees with our calculations. Through tuning the synthetic angles, we can flexibly design the TPB, which can be applied to realize filters with various bandwidths. In particular, narrowband optical filters can be achieved by magic angle pairs (the synthetic angles modulate an isolated TPB). The transmittance can be tailored by the thickness, and the surface flatness is further improved. However, we are more concerned about phenomena such as pulse delay, nonlinear effects, and pulse-width compression due to band compression.

As the TPB bandwidth is reduced, the group velocity can be reduced, which causes a pulse delay. The change of the pulse delay passing through the sample compared with the substrate is $\Delta\tau = (L_\alpha/v_g) - (L_\alpha/c) = (L_\alpha/c)(n_g - 1)$, where L_α is the thickness of the sample. If the influence of different L_α is ignored, the normalized pulse delay is $\Delta\tau_n = (n_g - 1)$, where n_g is the group index. In our experiment, a homemade optical setup is established to measure

TABLE I. Series of magic angle pairs (α_M, γ_M), which are the corresponding values of α and γ for g_M.

m	1	2	3	4	5	6	7
g_M	1.02	1.10	1.16	1.31	1.45	1.69	1.95
(α_M, γ_M)	(212.8°, 111.6°)	(269.6°, 89.8°)	(295.2°, 93.6°)	(309.6°, 87.2°)	(318.4°, 91.8°)	(324.8°, 86.4°)	(329.6°, 91.0°)
m	8	9	10	11	12	13	14
g_M	2.35	2.82	3.49	4.30	5.44	6.84	8.83
(α_M, γ_M)	(332.8°, 87.2°)	(336.0°, 90.8°)	(338.4°, 87.4°)	(340.0°, 90.6°)	(341.6°, 87.6°)	(343.2°, 90.4°)	(344.0°, 87.8°)

the pulse delay of the laser through multiphoton absorption by a silicon chip. The experimental setup for the pulse-delay measurement is shown in Fig. 5. It is based on a modified setup for measuring the relaxation time of carriers on silicon chips, which can generate time delays by shifting the optical path of the pump laser. However, here, we focus only on the jump in the reflection intensity of a silicon chip under the optical path change of the pump-pulse laser. We use a laser at 800 nm, which can be adjusted continuously as needed, with 120-fs pulse duration and 80-MHz repetition rate, and split a laser beam into two beams: one is the pump laser and the other is the probe laser. The pump laser passes through the β-barium borate (BBO) crystal, the wavelength of which becomes 400 nm, and then passes through the chopper, where the repetition rate is modulated to amplify the signal by the lock-in amplifier. After that, the pump laser passes through the motorized stage, which can continuously adjust the optical path of the pump laser, and then the pump laser illuminates the silicon chip with the probe laser. Meanwhile, the probe laser passes through the sample (moiré superlattices or substrate), of which we need to measure the pulse delay. The combined beam of the pump laser and probe laser illuminates the silicon chip, and then the reflectivity intensity of the probe laser is measured by the photodetector. Obviously, when the probe pulse illuminates the silicon chip earlier than the pump pulse, the reflection intensity is weaker due to the absorption of light by unexcited

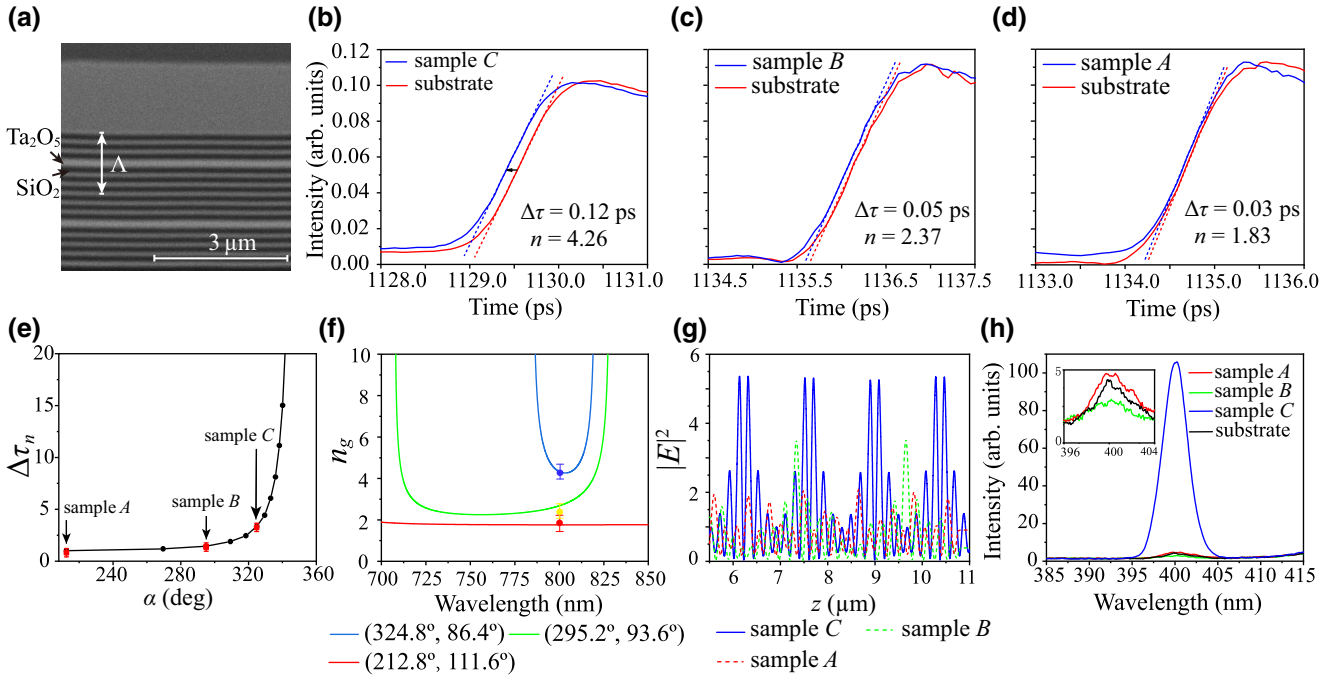

FIG. 4. (a) SEM microscopy picture of sample *C*. (b)–(d) Pulse time-delay measurement results. Red line is the transient reflection intensity of the silicon chip with the probe laser passing through the substrate. Blue line is the transient reflection intensity of the silicon chip with the probe laser passing through the moiré superlattices. (b) Sample *C*. (c) Sample *B*. (d) Sample *A*. Laser wavelength is 800 nm. (e) Pulse delay of different moiré superlattices; black dots are calculated data and red squares are the above-measured data of three samples. (f) Blue line is the group index on the TPB of the moiré superlattice with two synthetic angles (α, γ) (324.8°, 86.4°), green line is the group index on the TPB of the moiré superlattice with (295.2°, 93.6°), and red line is the group index on the TPB of the moiré superlattice with (212.8°, 111.6°). Red, green, and blue dots are experimental results. (g) Electric field distributions of samples *A*, *B*, and *C* at a wavelength of 800 nm. (h) SHG intensity of the samples and substrate.

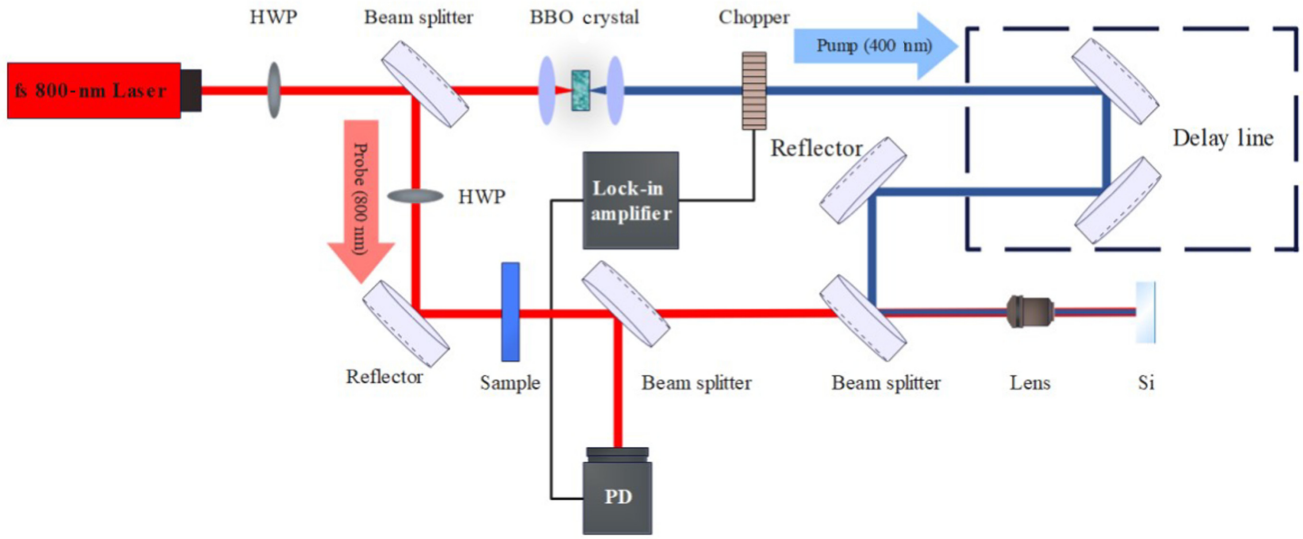

F5:1 FIG. 5. Schematic diagram of the experimental setup for measuring pulse time delay. Laser in the experiment is split into two beams
F5:2 through a beam splitter. One beam is called the pump laser (blue rays) after passing through a BBO crystal, which can multiplier the
F5:3 laser, and the other beam is called the probe laser (red rays). Pump laser can be delayed continuously by the delay line, which can be
F5:4 moved precisely, then the pump laser and probe laser are focused together on the Si chip by the objective lens, finally, reflected signal
F5:5 of the probe laser is collected by the photodetector. HWP, half-wave plate; PD, photodetector.

carriers in the silicon chip. As the motorized stage moves, the optical path difference between the pump laser and the probe laser decreases. When the probe laser illuminates the silicon chip later than the pump laser, the reflection intensity becomes stronger than before, because the silicon-chip carriers are excited by the pump laser. Therefore, we can observe the jump line of the reflection intensity in Figs. 4(b)–4(d). The time point of the jump is the position of the same optical path of the two beams, so the pulse-delay time is obtained through the motorized stage. In Figs. 4(b)–4(d), the red line is the spectrum of the silicon chip with the substrate placed in the optical path of the probe laser, and the blue line is the spectrum of the silicon chip with the moiré superlattice placed in the optical path of the probe laser. These blue lines move to the left due to the presence of the moiré superlattice.

When we place different samples on the light path of the probe laser, the optical path of the probe laser will change, and the position of the jump point will change. Therefore, we can obtain the pulse time delay according to the displacement of the jump point. For the setup error, the minimum measurement accuracy of the motorized stage is $\delta_l = 1\ \mu$m. Therefore, in the whole process, the pulse-delay theoretical error is $\delta_{\text{delay}} = (2\delta_l/c) \approx 0.01$ ps, where c is the speed of light in a vacuum.

In Fig. 4(b), the difference between the two lines is 0.12 ps, which is the measured pulse delay difference between sample C and the substrate. In this way, we can also measure the pulse delay of the other two samples in Figs. 4(c) and 4(d). In Fig. 4(e), experimental data agree well with the calculated $\Delta\tau_n$ results. It can be seen that the increase of g results in an increase of pulse delays. Meanwhile, we use the pulse-delay measurement results to obtain the group index. As shown in Fig. 4(f), the red, green, and blue lines correspond to the group indices on different TPBs of moiré superlattices, and the red, green, and blue dots are experimental data, which are obtained according to the pulse delay. Slow light with a large group index and lower group velocity has potential applications in optical buffering and advanced time-domain optical signal processing. Slow light compresses optical energy in space, which enhances linear and nonlinear effects, and so, miniaturizes functional photonic devices.

Band compression also leads to field enhancement, which enhances the nonlinear optical effect. In Fig. 4(g), we calculate the transmission electric field distribution at a wavelength on the TPB of different moiré superlattices. The electric field of the moiré superlattice with (324.8°, 86.4°) is stronger near 800 nm. This enables an enhancement of the nonlinear effect. In experiments, we input an 800-nm laser into the three samples, and the produced second-harmonic generation (SHG) is measured, as shown in Fig. 4(h). Under the same incident laser intensity, the SHG generated by sample C is enhanced nearly 50 times more than the substrate. However, for sample B, since the frequency of SHG is inside the band gap, the SHG is weaker than the substrate. The experimental results can be well explained by the calculated results of field enhancement on the TPB. This also suggests that

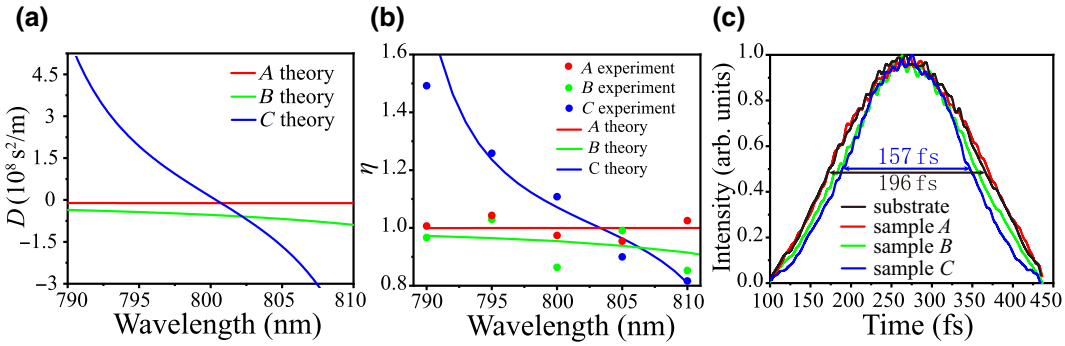

F6:1 FIG. 6. (a) Blue line is the group-velocity dispersion on the TPB of the moiré superlattice with two synthetic angles (α, γ) (324.8°,
F6:2 86.4°), green line is the group-velocity dispersion on the TPB of the moiré superlattice with (295.2°, 93.6°), and red line is the group-
F6:3 velocity dispersion on the TPB of the moiré superlattice with (212.8°, 111.6°). (b) Pulse-width rate before and after the laser passes
F6:4 through the moiré superlattices on the TPB. Solid line is the theoretical calculation results; dots are experimental results. (c) Laser-
F6:5 pulse profiles. Black line is the original pulse profile through the substrate, red line is the original pulse profile through sample *A*, green
F6:6 line is the pulse profile through sample *B*, and blue line is the pulse profile through sample *C*. Laser wavelength is 810 nm.

slow light can enhance light-matter interactions, such as nonlinearities on the TPB, and the moiré superlattices enable the multiplication of the laser frequency to produce the SHG.

Meanwhile, we also measure the pulse shape of the laser, and the results show that, due to a stronger negative group-velocity dispersion, the pulse width is compressed by the TPB. We also analyze the variation of the pulses of the laser passing through the moiré superlattice. Variation in pulse width is affected by the group-velocity dispersion on the TPBs of the moiré superlattices. We obtain the pulse-width-variation ($\Delta\tau_p$) formula:

$$\Delta\tau_p = D(\omega)L_\alpha\Delta\omega, \tag{3}$$

where $D(\omega) = d(1/v_g)/d\omega$ is the group-velocity dispersion, v_g is the group velocity, L_α is thickness of the sample, and $\Delta\omega$ is the pulse spectral width. We define the pulse-width rate as $\eta = (\tau_0 + \Delta\tau_p)/\tau_0$, where τ_0 is the initial laser-pulse width. In Fig. 6(a), we calculate the group-velocity dispersion on TPBs for several moiré superlattice samples. Furthermore, from Eq. (3), we calculate the pulse-width rate, η, and compare it with the experimental results, which are measured by an autocorrelator in Fig. 6(b). Over a certain wavelength range, the pulse width with a large α changes more drastically. In Fig. 6(c), comparing the pulse after passing through the moiré superlattice with that through the substrate, we demonstrate that the moiré superlattice has an effect of compressing the pulse width. At a wavelength of 810 nm, sample *C* produces more pulse-width compression than the other two samples; this is due to the larger negative group-velocity dispersion at 810 nm. The properties of the moiré superlattice can also be used to fabricate a compact compressor for laser pulses. The pulse compressor allows the optical pulse to transform or maintain an ultrashort optical pulse during propagation, which will benefit ultrafast optical communications, optical signal processing, and noncommunication applications.

V. CONCLUSION AND DISCUSSION

We propose a method of constructing photonic moiré superlattices with two synthetic twist angles. A two-dimensional synthetic moiré sphere is constructed based on these two angles, which gives all possible structural parameters of the moiré superlattice. We find a series of magic angle pairs, corresponding to TPBs with optimal band compression. Meanwhile, the one-dimensional moiré superlattices offer advantages of convenient fabrication and low costs. Experimentally, a method to measure the pulse delay caused by the slow-light effect on the TPB of moiré superlattices by measuring the transient reflection spectrum on a silicon chip is proposed, and the enhancement of the SHG in the TPB is analyzed. The research results show that band compression leads to many interesting phenomena, such as pulse delay, pulse-width compression, and nonlinear effects. High-dimensional moiré superlattices with synthetic multitwist angles exhibit many physical properties and physical phenomena. We believe that the method to design synthetic multitwist angles can be extended to other systems, and many other synthetic moiré superlattices can be realized. Some other interesting applications are possible based on revealing peculiar optical properties.

ACKNOWLEDGMENTS

This work is financially supported by the National Natural Science Foundation of China (Grants No. 92163216 and No. 92150302).

[1] O. Kafri and I. Glatt, *The Physics of Moire Metrology* (John Wiley & Sons Inc, New York, 1990).

[2] R. Bistritzer and A. H. MacDonald, Moire bands in twisted double-layer graphene, Proc. Natl. Acad. Sci. U. S. A. **108**, 12233 (2011).

[3] Z. Song, Z. Wang, W. Shi, G. Li, C. Fang, and B. A. Bernevig, All Magic Angles in Twisted Bilayer Graphene are Topological, Phys. Rev. Lett. **123**, 036401 (2019).

[4] G. Tarnopolsky, A. J. Kruchkov, and A. Vishwanath, Origin of Magic Angles in Twisted Bilayer Graphene, Phys. Rev. Lett. **122**, 106405 (2019).

[5] Y. Cao, V. Fatemi, A. Demir, S. Fang, S. L. Tomarken, J. Y. Luo, J. D. Sanchez-Yamagishi, K. Watanabe, T. Taniguchi, E. Kaxiras, *et al.*, Correlated insulator behaviour at half-filling in magic-angle graphene superlattices, Nature **556**, 80 (2018).

[6] H. S. Arora, R. Polski, Y. Zhang, A. Thomson, Y. Choi, H. Kim, Z. Lin, I. Z. Wilson, X. Xu, J. H. Chu, *et al.*, Superconductivity in metallic twisted bilayer graphene stabilized by WSe2, Nature **583**, 379 (2020).

[7] P. Stepanov, I. Das, X. Lu, A. Fahimniya, K. Watanabe, T. Taniguchi, F. H. L. Koppens, J. Lischner, L. Levitov, and D. K. Efetov, Untying the insulating and superconducting orders in magic-angle graphene, Nature **583**, 375 (2020).

[8] S. Wu, Z. Zhang, K. Watanabe, T. Taniguchi, and E. Y. Andrei, Chern insulators, van Hove singularities and topological flat bands in magic-angle twisted bilayer graphene, Nat. Mater. **20**, 488 (2021).

[9] K. Tran, G. Moody, F. Wu, X. Lu, J. Choi, K. Kim, A. Rai, D. A. Sanchez, J. Quan, A. Singh, *et al.*, Evidence for moire excitons in van der Waals heterostructures, Nature **567**, 71 (2019).

[10] A. Abouelkomsan, Z. Liu, and E. J. Bergholtz, Particle-Hole Duality, Emergent Fermi Liquids, and Fractional Chern Insulators in Moire Flatbands, Phys. Rev. Lett. **124**, 106803 (2020).

[11] A. Timmel and E. J. Mele, Dirac-Harper Theory for One-Dimensional Moire Superlattices, Phys. Rev. Lett. **125**, 166803 (2020).

[12] J. B. Khurgin, Light slowing down in Moiré fiber gratings and its implications for nonlinear optics, Phys. Rev. A **62**, 013821 (2000).

[13] A. Kocabas, S. S. Senlik, and A. Aydinli, Slowing down surface plasmons on a moire surface, Phys. Rev. Lett. **102**, 063901 (2009).

[14] P. Wang, Y. Zheng, X. Chen, C. Huang, Y. V. Kartashov, L. Torner, V. V. Konotop, and F. Ye, Localization and delocalization of light in photonic moire lattices, Nature **577**, 42 (2020).

[15] G. Hu, Q. Ou, G. Si, Y. Wu, J. Wu, Z. Dai, A. Krasnok, Y. Mazor, Q. Zhang, Q. Bao, *et al.*, Topological polaritons and photonic magic angles in twisted alpha-MoO3 bilayers, Nature **582**, 209 (2020).

[16] M. Chen, X. Lin, T. H. Dinh, Z. Zheng, J. Shen, Q. Ma, H. Chen, P. Jarillo-Herrero, and S. Dai, Configurable phonon polaritons in twisted alpha-MoO3, Nat. Mater. **19**, 1307 (2020).

[17] Q. Fu, P. Wang, C. Huang, Y. V. Kartashov, L. Torner, V. V. Konotop, and F. Ye, Optical soliton formation controlled by angle twisting in photonic moiré lattices, Nat. Photonics **14**, 663 (2020).

[18] Y. V. Kartashov, F. Ye, V. V. Konotop, and L. Torner, Multifrequency Solitons in Commensurate-Incommensurate Photonic Moire Lattices, Phys. Rev. Lett. **127**, 163902 (2021).

[19] X. R. Mao, Z. K. Shao, H. Y. Luan, S. L. Wang, and R. M. Ma, Magic-angle lasers in nanostructured moire superlattice, Nat. Nanotechnol. **16**, 1099 (2021).

[20] K. Dong, T. Zhang, J. Li, Q. Wang, F. Yang, Y. Rho, D. Wang, C. P. Grigoropoulos, J. Wu, and J. Yao, Flat Bands in Magic-Angle Bilayer Photonic Crystals at Small Twists, Phys. Rev. Lett. **126**, 223601 (2021).

[21] X. Lin, Z. Liu, T. Stauber, G. Gomez-Santos, F. Gao, H. Chen, B. Zhang, and T. Low, Chiral Plasmons with Twisted Atomic Bilayers, Phys. Rev. Lett. **125**, 077401 (2020).

[22] B. Lou, N. Zhao, M. Minkov, C. Guo, M. Orenstein, and S. Fan, Theory for Twisted Bilayer Photonic Crystal Slabs, Phys. Rev. Lett. **126**, 136101 (2021).

[23] A. Regensburger, C. Bersch, M. A. Miri, G. Onishchukov, D. N. Christodoulides, and U. Peschel, Parity-time synthetic photonic lattices, Nature **488**, 167 (2012).

[24] A. Celi, P. Massignan, J. Ruseckas, N. Goldman, I. B. Spielman, G. Juzeliunas, and M. Lewenstein, Synthetic Gauge Fields in Synthetic Dimensions, Phys. Rev. Lett. **112**, 043001 (2014).

[25] X. W. Luo, X. Zhou, C. F. Li, J. S. Xu, G. C. Guo, and Z. W. Zhou, Quantum simulation of 2D topological physics in a 1D array of optical cavities, Nat. Commun. **6**, 7704 (2015).

[26] T. Ozawa, H. M. Price, N. Goldman, O. Zilberberg, and I. Carusotto, Synthetic dimensions in integrated photonics: From optical isolation to four-dimensional quantum Hall physics, Phys. Rev. A **93**, 043827 (2016).

[27] L. F. Livi, G. Cappellini, M. Diem, L. Franchi, C. Clivati, M. Frittelli, F. Levi, D. Calonico, J. Catani, M. Inguscio, *et al.*, Synthetic Dimensions and Spin-Orbit Coupling with an Optical Clock Transition, Phys. Rev. Lett. **117**, 220401 (2016).

[28] Q. Lin, M. Xiao, L. Yuan, and S. Fan, Photonic Weyl point in a two-dimensional resonator lattice with a synthetic frequency dimension, Nat. Commun. **7**, 13731 (2016).

[29] Q. Wang, M. Xiao, H. Liu, S. Zhu, and C. T. Chan, Optical Interface States Protected by Synthetic Weyl Points, Phys. Rev. X **7**, 031032 (2017).

[30] O. Zilberberg, S. Huang, J. Guglielmon, M. Wang, K. P. Chen, Y. E. Kraus, and M. C. Rechtsman, Photonic topological boundary pumping as a probe of 4D quantum Hall physics, Nature **553**, 59 (2018).

[31] L. Yuan, Q. Lin, M. Xiao, and S. Fan, Synthetic dimension in photonics, Optica **5**, 1396 (2018).

[32] E. Lustig, S. Weimann, Y. Plotnik, Y. Lumer, M. A. Bandres, A. Szameit, and M. Segev, Photonic topological insulator in synthetic dimensions, Nature **567**, 356 (2019).

[33] A. Dutt, Q. Lin, L. Q. Yuan, M. Minkov, M. Xiao, and S. H. Fan, A single photonic cavity with two independent physical synthetic dimensions, Science **367**, 59 (2020).

[34] See the Supplemental Material at http://link.aps.org/supplemental/10.1103/PhysRevApplied.0.XXXXXX for (1) band-evolution analysis near the TPB, (2) experimental samples and their transmission spectra on the TPB, and (3) the effect of oblique incidence on the group index on the TPB.